HYDROSTATIC 3D-PRINTING FOR SOFT MATERIAL STRUCTURES USING LOW ONE-PHOTON POLYMERIZATION

A Thesis

by

DONG SUNG KIM

Submitted to the Office of Graduate and Professional Studies of
Texas A&M University
in partial fulfillment of the requirements for the degree of

MASTER OF SCIENCE

Chair of Committee,	Bruce Tai
Committee Members,	Jyhwen Wang
	Melissa Grunlan
Head of Department,	Andreas A. Polycarpou

August 2016

Major Subject: Mechanical Engineering

ABSTRACT

Three-dimensional soft structures are difficult to fabricate without any supporting materials in additive manufacturing due to their extremely low stiffness against gravity. This study presents the feasibility of a conceptual 3D printing method that enables a hydrostatic condition and eventually achieves support-free fabrication, named hydrostatic 3D printing (H3P).

Hydrostatic 3D printing utilizes low one-photon polymerization (LOPP) to realize polymerization under the polymer resin surface, as opposed to surface polymerization in stereolithography (SLA). The cured part inside of the resin is then automatically supported by the hydrostatic pressure. A preliminary study was designed to observe LOPP of a UV curable silicone material at a wavelength of 365 nm. A single-spot curing and a continuous printing were both investigated under different light intensities and exposure times. The equivalent exposure time for LOPP in a continuous printing was found to be much shorter than a stationary single-spot curing due to a non-linear intensity distribution. Initial results have demonstrated the feasibility of hydrostatic printing using LOPP while also revealing the challenges of hydrostatic 3D printing.

ACKNOWLEDGEMENTS

I would like to thank the committee chair, Dr. Bruce Tai and the committee members, Dr. Jyhwen Wang and Dr. Melissa Grunlan for their guidance and support throughout the process of this research.

Thanks also go to my friends and colleagues and the department faculty and staff for making my time at Texas A&M University a great experience.

Finally, thanks to my kids, Joohwan and Yehwan for their love and to my wife, Jin Soo for her sacrifice and love.

TABLE OF CONTENTS

LIST OF FIGURES

1. INTRODUCTION

1.1. Motivation

Additive manufacturing (AM) technologies have been advanced in the past decade to be capable of fabricating a wide variety of materials into the 3D configuration, such as plaster powders, thermal plastics, photopolymers, to metal alloys. Recent advancements have also enabled gradient materials by mixing different ratios of polymer resin which can achieve the various hardness. Applications have also been broadened from simply display, toys, to functional uses. However, additive manufacturing cannot completely replace the conventional techniques due to the requirements of surface finish, tolerances, or the constraint from the material property itself. One of challenging issue is printing ultra-soft, jelly like materials, particularly those can hardly support their body weights, such as silicone and gellan gum [1]. Soft material is useful for biomedical applications such as making synthetic tissues, encapsulation of drugs or sensors, soft surgical robotics, developing and training for surgical methods, producing replicas with each patient's data or medical treatment in the human body [2], [3], [4], [5], [6].

The common conventional technique for soft matters is a molding process due to relatively simple and economical process. However, it cannot create enclosed cavities in the structure as a one-piece structure, such as vessel lumen, brain ventricles, and heart ventricles/atriums shown in Fig. 1. Therefore, additive manufacturing process can be utilized to overcome the limitation in soft material manufacturing, and then achieve more accurate and user-based designs. However, depending on the solidification method, printing such soft materials could require a substantial amount of support structure to

ensure the part integrity as shown in Fig.2. Using support structures is common in 3D printing, but it requires a post processing to remove the support material. Some, or all, of the post-processing procedures are not suitable for soft and fragile materials. For example, fused deposition modeling (FDM) employs a soluble support material to build the overhang structures. The support structure will be dissolved in an agitated base solution. In stereolithography (SLA), the support structure is printed simultaneously with the part in the liquid resin and trimmed manually after printing. Commercial UV-based products, such as Connex machines (Stratasys, Edina, MN), use water-soluble wax as the support material and needs to be cleaned with high-pressure water blasting system.

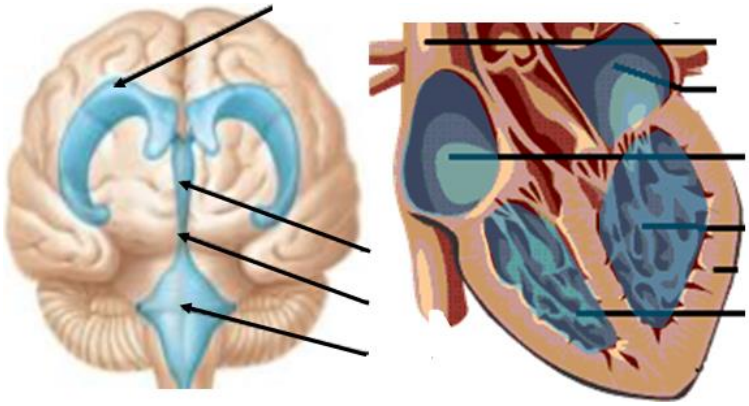

Figure 1. Enclosed cavities, ventricles/atrium, in the brain (left) and heart (right).

Furthermore, fully removing the support structure inside the deep cavity, internal void, or channels are technically difficult and time-consuming. To address these issues, this study is presenting a novel, support-free, soft material fabrication method in additive manufacturing.

Figure 2. 3D printed nasal prosthetics [7].

1.2. Support-free fabrication

The key concept of the support-free fabrication is to create a hydrostatic condition for the solidified material and to eliminate the conventional layer-by-layer manner as shown in Fig.3. The hydrostatic condition enables for the structures to maintain their positions and shapes without any support structures. This is a similar approach to powder-bed printing technologies such as selective laser sintering (SLS). SLS generally does not build any support structure since the part is immersed in the powder bed and directly sintered with the supports from surrounding loose powders as shown in Fig.4. The non-layering technique is inspired from the 3D stereo drawing pen [8], so that the overhang structure can be fabricated as a continuous piece at a time as shown in Fig.5.

Creating a hydrostatic condition is challenging. SLA and digital light processing (DLP) technologies both utilize UV light to cure the part in a resin bath. However, they do not necessarily create a hydrostatic environment for several reasons. First of all, the curing process is layer-by-layer from the surface or from the bottom, meaning that the

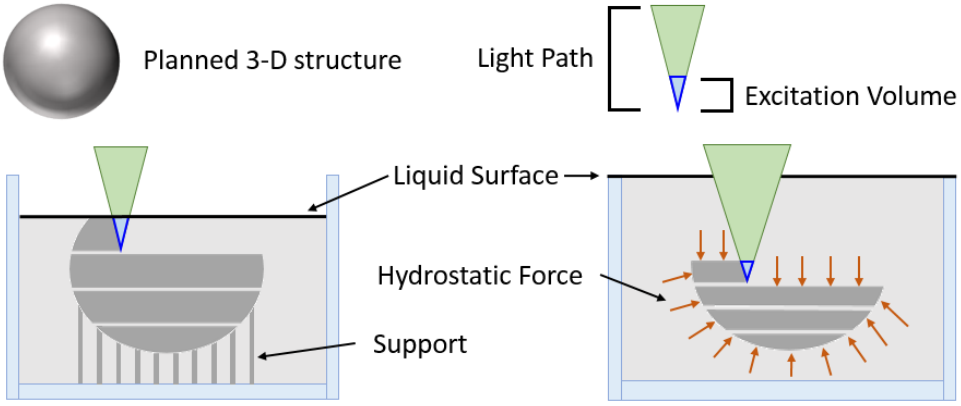

Figure 3. Schematic comparisons between (a) stereolithography (SLA) and (b) hydrostatic 3D-printing.

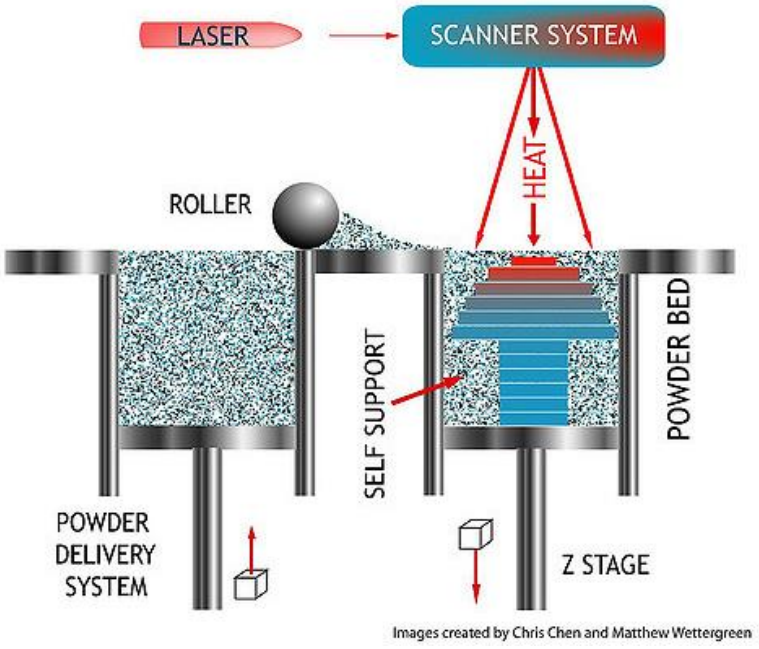

Figure 4. Schematic diagram of selective laser sintering (SLS) [9].

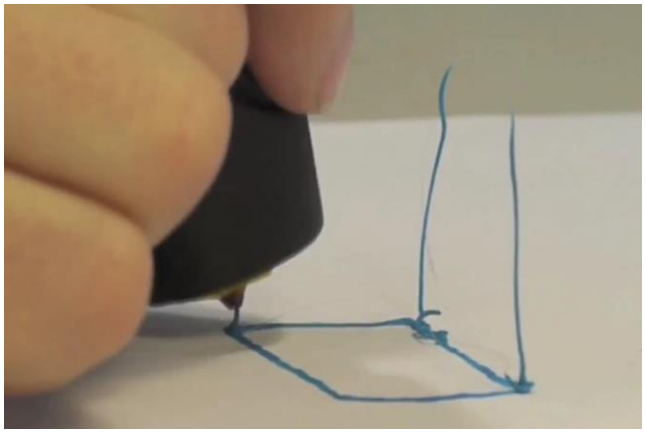

Figure 5. Demonstration of the 3Doodler pen [10].

part is not completely immersed in the middle of the bath as shown in Fig.6 [11], [12]. Second, both technologies require continuous movement of the printing base to form a 3D geometry. The movement can cause that the liquid resin disturbs a soft body to stay in the shape. Lastly, the cured portion may have a significantly different (heavier) density that can only be partially supported the uncured resin.

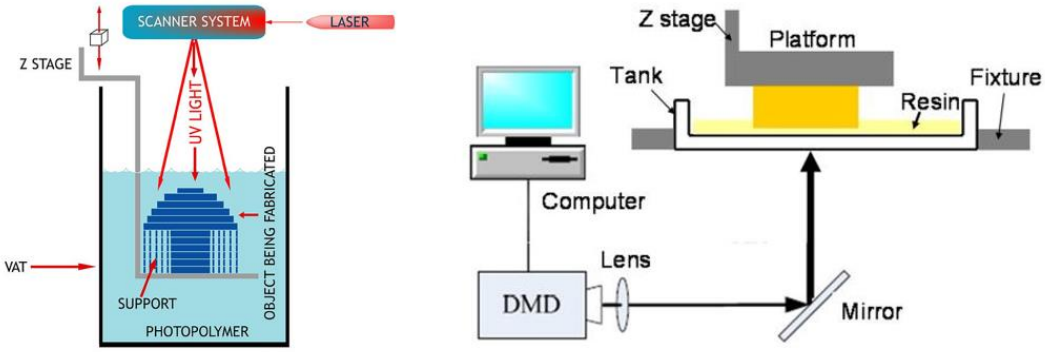

(a) (b)

Figure 6. Typical approaches for SLA (a) top-down [13] and (b) bottom-up [14].

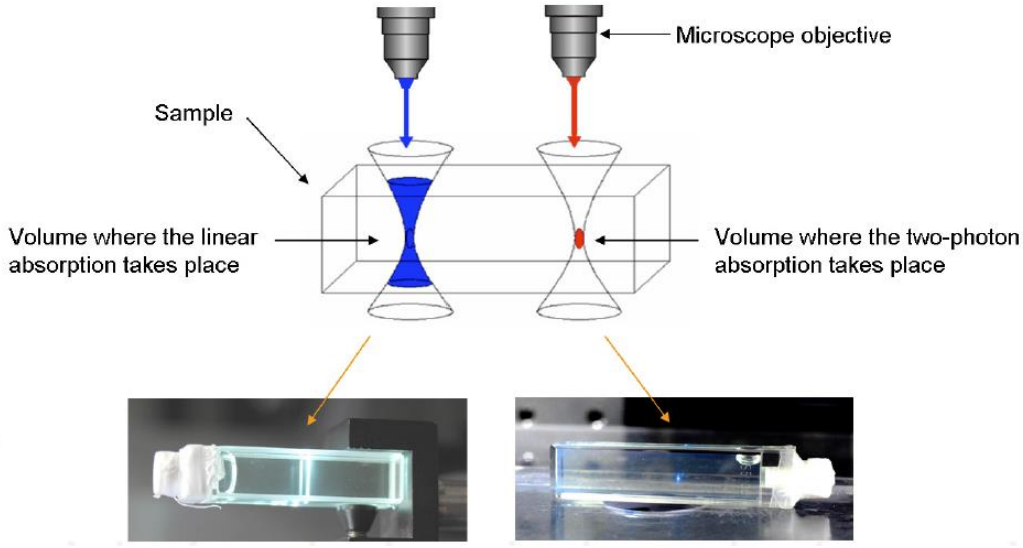

Figure 7. Comparison of the excitation volumes for the one-photon absorption (left) and two-photon absorption (right) [15].

To achieve the hydrostatic condition during the process, UV light must cure the part from the middle of the liquid bath. However, a single wavelength UV light (i.e., one-photon polymerization (OPP)) results in curing along the entire beam path as shown in Fig.7. Therefore, two-photon polymerization (TPP) could be one of the alternatives. TPP is a non-linear process to realize the curing process only at the focal point as shown in Fig.7 [16], [17]. However, this technique requires complex configurations and high-cost optical devices such as ultrashort pulsed lasers. All of these make TPP less practical in the additive manufacturing market. Instead, a similar TPP can be achieved using low one-photon polymerization (LOPP).

Low one-photon polymerization effect is proposed in [18], which utilizes low absorption rates of photoresists and wide beam gradient with high numerical aperture (N.A.). The photoresists have specific absorption rates depending on wavelengths. In

general, one-photon polymerization process utilizes the wavelengths that the photoresists have high absorption rates. In contrast, low one-photon polymerization uses the wavelengths that the photoresists have relatively very low absorption rates [19]. Using the low absorption rates of the photoresists prevents the polymerization along with the beam path, thus to realize the focal curing effect of TPP. However, a successful LOPP requires precise controls over the wavelength, intensity, exposure time, and known polymerization properties.

1.3. Objective

The objective of this study is to investigate the feasibility of low one-photon polymerization to realize a hydrostatic 3D printing of silicone material. To address this point, the optical features of the silicone material was studied and a test bed with the optical array was developed. The preliminary study was conducted to verify the parameters such as wavelengths, intensities and exposure times. Based on the study, stationary single-spot testing and continuous printing will be carried out.

2. TESTBED DEVELOPMENT

In this section, testbed development to achieve LOPP and hydrostatic condition will be presented. It is important to design a proper optical setup according to material selection. Especially, the absorbance of the material plays a key role to decide the specification of the setup for LOPP.

2.1. UV curable silicone

To verify the concept and feasibility of a hydrostatic 3D printing, this study used a non-commercialized UV curable silicone material from Dow Corning (Midland, MI). The UV curable silicone resin was made by mixing two parts as shown in Fig.8. One was the silicon resin, and the other was the photo-initiator. The initiator is activated by a certain range of UV wavelength. The initiator plays a major role in the polymerization. The absorption spectrum of the photo-imitator was measured by using a spectrophotometer (U-4100, Hitachi, Tokyo, Japan) and presented in Fig. 9. The sample was diluted to 10.5 %wt. by the solvent. The optical path length was 1 cm. The measured range of wavelengths was between 300 nm and 500 nm. The absorption began around 400 nm wavelength down to 300 nm and below. The wavelength of 365 nm was selected in this study because it had a low absorption value 0.051, but not extremely low, and was a common band pass filter that can be easily obtained. A longer wavelength toward 400 nm can lead to lower absorption but also could require a significant amount of time to cure the silicone or could not initiate the curing process due to insufficient energy absorption.

To realize the hydrostatic support-free fabrication, the silicone resin must have a minimum difference in density before and after polymerization (i.e., cured and uncured silicone). This is because a large difference can cause the motion of the cured part as a result of gravity against buoyancy force. The physical properties were not disclosed by the silicone supplier, but the measured densities of liquid and solid phases were found both around 0.97 g/ml. The other important physical property is viscosity. A viscous liquid material provides resistance against the motion inside the liquid. Along with the similar density, high viscosity can further improve the stability of the cured part.

Figure 8. Picture for two parts of the UV curable silicone

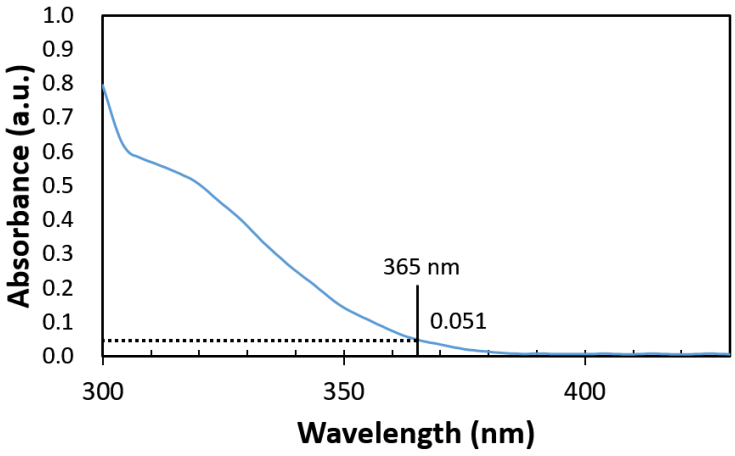

Figure 9. Absorption spectrum of the photo-initiator.

2.2. Testbed development

The overall experimental setup is shown in Fig. 10. The setup consists of a UV lamp system (OmniCure S2000, Excelitas Technologies Corp., Waltham, MA), the optical lens array, and the 3-axis reconfigurable motion stage (Moog Animatics, Milpitas, CA). The whole setup is covered by amber plates to block the UV wavelength from the environment.

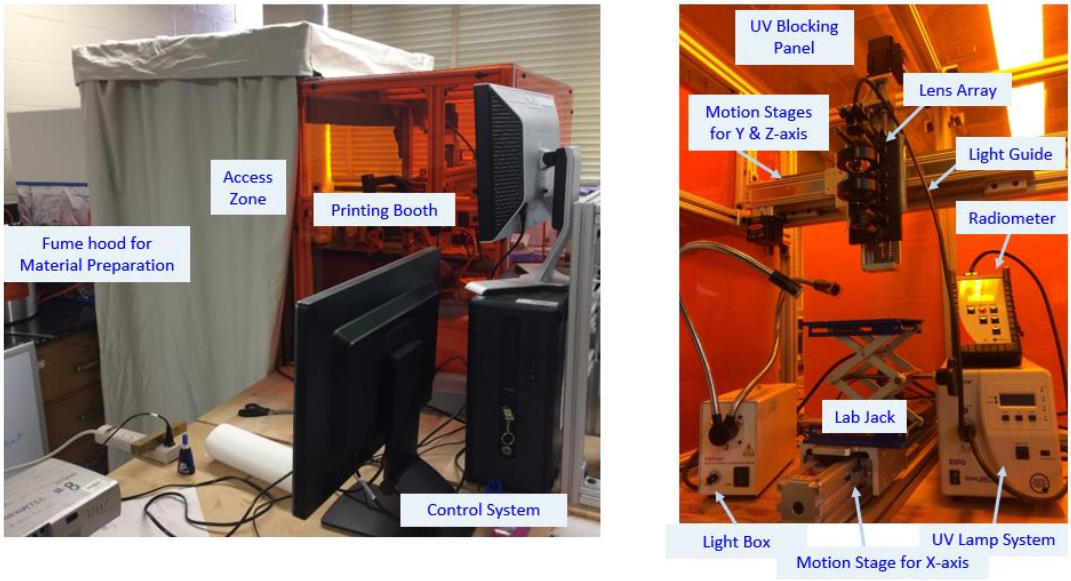

Figure 10. Experimental testbed: (a) the overall setup, (b) devices in the printing booth.

The lamp system has a wide beam spectrum from 250 nm to 650 nm. A bandpass filter can be added to provide a sole wavelength of 365 nm from the lamp system. The lens array is composed of the aspheric lenses (Edmund Optics Inc., Barrington, NJ), the bandpass filter (Edmund Optics Inc., Barrington, NJ), and iris diaphragms (Edmund Optics Inc., Barrington, NJ) as shown in Fig. 11. The aspheric lenses are used for

collimating and focusing the beam with the magnification 1/5 that produces the focal spot with 1 mm diameter. In addition, to realize wide beam gradient, the aspheric lens with the numerical aperture (N.A) = 1 is used as the focusing lens. The iris diaphragms are used to align the beam. The beam intensity is controlled by the electrical shutter of the lamp system that changes the iris opening from 1 % to 100 %. Note that the actual output light intensity is not linearly proportional to the iris opening. For example, 70% opening does not necessarily mean a 70% intensity of the fully opened iris. Therefore, the actual energy dose (intensity multiplies exposure time) needs to be calibrated with the irradiance values measured by a radiometer. Using the dual light guide, the beam from the system can be connected simultaneously with the lens array and the radiometer (R2000, Excelitas Technologies Corp., Waltham, MA).

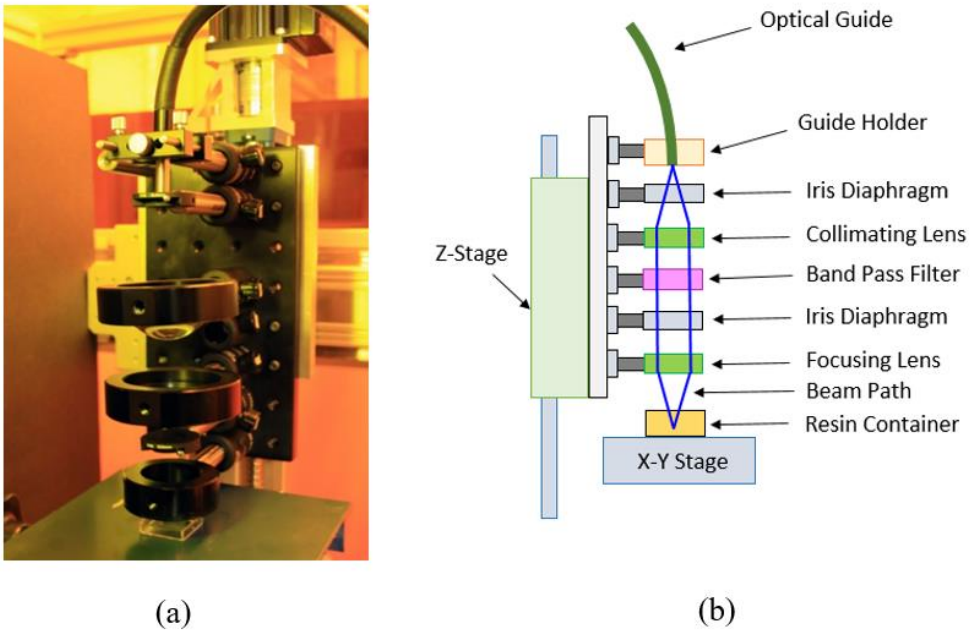

Figure 11. Lens array: (a) actual picture, (b) schematic diagram.

A wide beam gradient is one important factor to realize LOPP. However, lenses with high numerical aperture (NA) have a short focal length. In this testbed, the focusing lens has the back focal length (BFL) of 6.9 mm

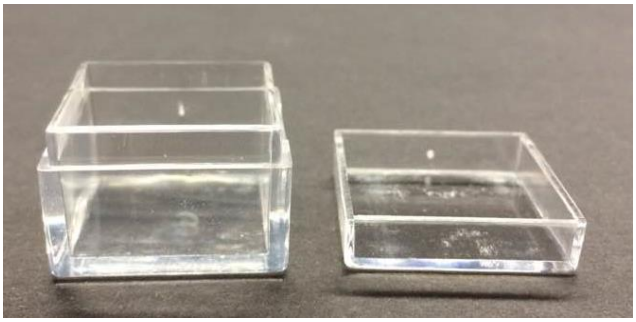

Figure 12. Acrylic boxes as a silicone resin container.

The light box (with UV wavelength blocked) is used to observe the fabrication process. The X, Y, Z-axis motion stages enable three dimensional motions for the fabrication purpose. The entire system is built by 8020 aluminum frames and linear sliders that have a resolution of 2.5 μm and can be numerically controlled using G-codes. Small acrylic boxes (with the external dimensions of 25.4 mm × 25.4 mm × 16.4 mm and 25.4 mm × 25.4 mm × 6.3 mm as shown in Fig. 12 are used as a silicone resin container. Given the current optical setup with BFL = 6.9 mm, the acrylic box needs to be placed close to the last aspheric lens to ensure the focal point inside the liquid for hydrostatic printing. The lab jack is used for coarse adjustment of sample height.

3. OBSERVING LOPP IN SILICONE RESIN

In this part, preliminary test and single spot test will be discussed. To verify LOPP effect, the qualitative observation and quantitative measurement were conducted.

The qualitative observation is designed to create different cured volumes under different intensities and exposure times, based on trial-and-error, for proof of LOPP concept. The quantitative one is to find the effects of light intensity and exposure time on creating LOPP.

3.1. Experiment I: observation of LOPP

3.1.1. Methods

The preliminary experimental study was conducted to demonstrate low one-photon polymerization (LOPP). Fig. 13 shows the schematics of one-photon polymerization (OPP) and LOPP. As mentioned in previous part, OPP occurs along the entire beam path due to high-rate absorption of UV light regardless the gradient light intensity. In contrast, LOPP takes place from the focal point. With the low-rate absorption, the curing time is dominated by the light intensity along the gradient beam path. Therefore, the curing can be controlled with a proper exposure time.

To verify LOPP in this experiment, an H-shape structure was tried for observation as shown in Fig. 14. The cured part was completely transparent and cannot be seen within the silicone resin. Thus, the remaining liquid must be drained out in order to observe polymerized parts.

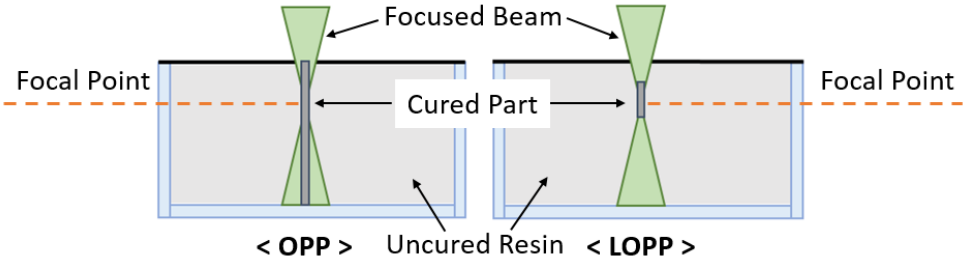

Figure 13. Schematic diagram of one-photon polymerization (OPP) and low one-photon polymerization (LOPP).

The H-shape structure was fabricated with the direction from the left to the right. The long left pillar was built by a high intensity and long exposure time to create OPP effect and then switched to a shorter exposure and lower intensity to create an LOPP bridge part. Two iris opening powers, 100% and 70%, were used for different intensities. The feed rate of the light source, controlled by the motion stage, was used to determine the exposure time in the unit of second per millimeter. Finally, another long exposure was used to create the right pillar of the H-shape. Although the bridge part created by LOPP could exist alone under the hydrostatic condition, it cannot be observed due to the transparency before the liquid resin was drained out. Therefore, the long pillars of the H-shape were needed to secure the structure inside the resin container for the purpose of observation.

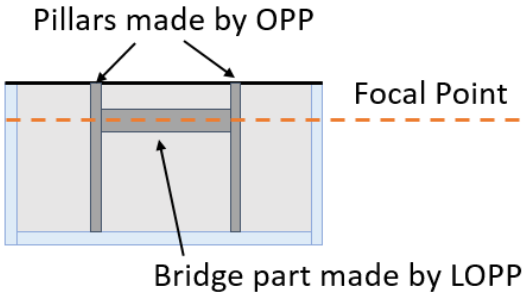

Figure 14. Printing of H-shape structure for proof of LOPP concept

3.1.2. Results

Figure 15 shows the results of printed H-shape structures. Under the fabrication conditions with 100% opening power and exposure time of 60 s/mm, the entire structure was generated only by OPP due to high intensity and long exposure time, shown in Fig. 15 (a) where the bridge portion was not seen. By reducing the exposure time to 30 s/mm, the structure was still made with OPP. However, because of a shorter exposure time, the bridge portion had a thinner thickness as shown in Fig. 15 (b). Since the top of the structure is lined up with the liquid surface, it means that a short exposure time is likely to result in a limited penetration depth, instead of being LOPP. By reducing the beam intensity to 70% opening and maintaining the short exposure time at 30 s/mm, there was no bridge portion between the pillars. With an increased exposure time to 55 s/mm at 70% opening power, the bridge structure then was formed again, as shown in Fig. 15 (c). The bridge portion might contain both OPP and LOPP effects. The bridge portion with a gap from the liquid surface could be considered LOPP. The extra solid area on the middle part is possibly produced by OPP.

At this point, it was difficult to distinguish LOPP and OPP effects mainly due to the limitation of the limited working distance of the final lens (i.e., BFL = 6.9 mm.) With the geometrical constraints from the lens frame and resin container, the focal point was approximately 3 to 4 mm below the liquid surface. To overcome a vague boundary between LOPP and OPP effects, a stationary single-spot testing and continuous printing were designed and conducted. The details are presented in the next sections.

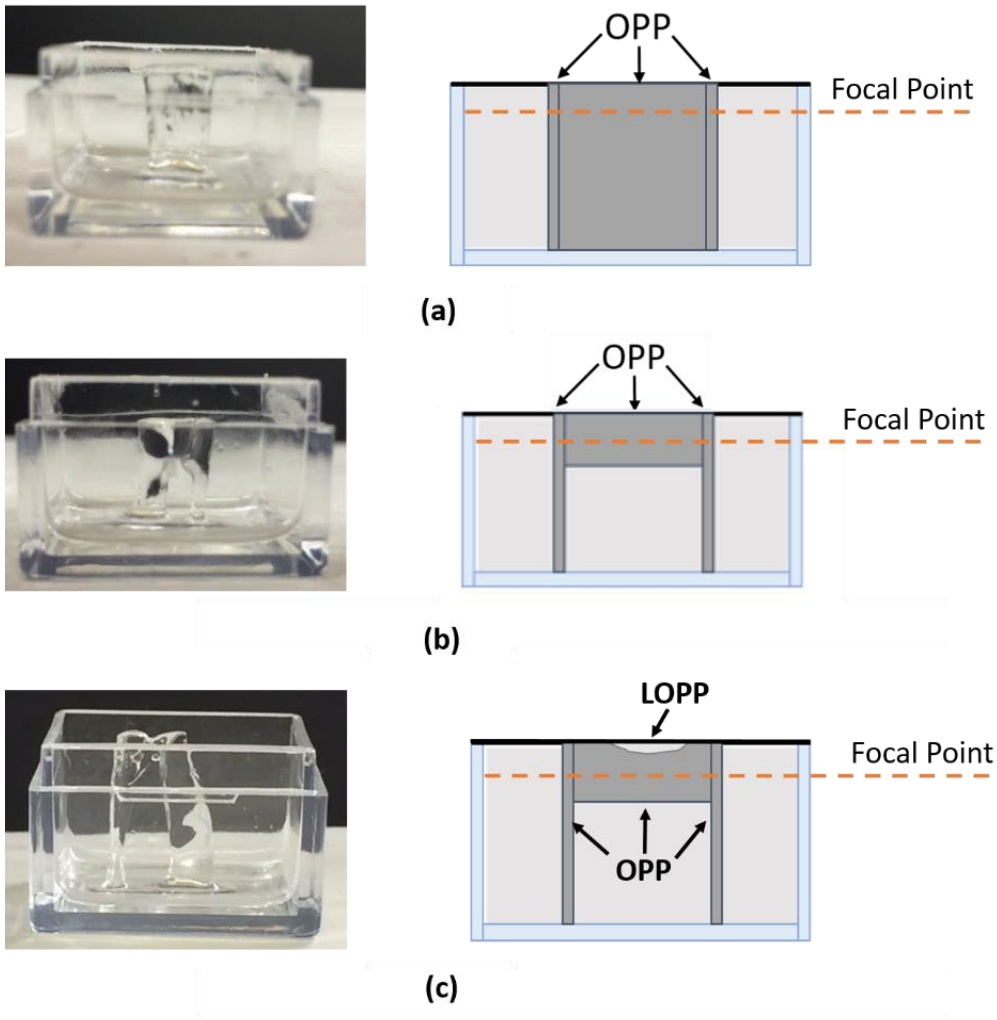

Figure 15. Observation results: (a) the structure under the fabrication conditions with 100 % opening power and exposure time 60 s/mm, (b) with 100 % opening power and exposure time of 30 s/mm, and (c) with 70 % opening power and exposure time of 55 s/mm.

3.2. Experiment II: single-spot test for LOPP

3.2.1. Method

This experiment was designed to measure the LOPP effect quantitatively without the unclear boundary between OPP and LOPP that observed in the preliminary experiment.

With the consideration of BFL = 6.9 mm of the focusing lens in the optical setup, a shallower acrylic container (4.9 mm in depth) was used in different from the container in the preliminary experiment as shown in Fig. 16. The small depth enabled that the focal point could be lined up near the bottom surface. This way allowed the cured part to have adhesion to the bottom of the resin container. The adhesion prevented from the part's missing and moving after the resin was drained out for the observation.

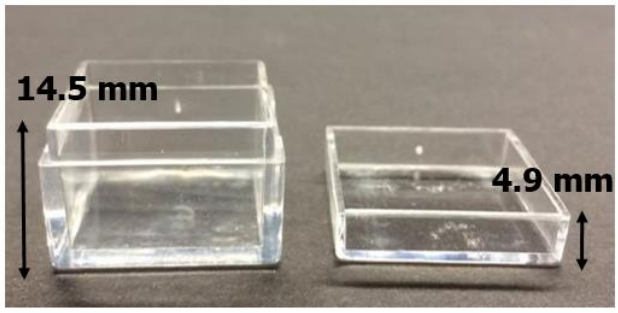

Figure 16. Resin containers: for preliminary experiment (left) and for stationary test (right)

As shown in Fig. 17, OPP creates a 4.9 mm full-length pillar through the liquid bath. On the other hand, LOPP only makes shorter pillars than 4.9 mm. By measuring the heights of the cured pillars, OPP and LOPP can be verified. This study was conducted by changing the intensity and exposure time. Two intensities with 100% opening and 70% opening were used. For the 100% opening power, the exposure time was increased every 5 s in an ascending order up to 80s. For the 70% opening power, the exposure time was increased every 10 s up to 200 s. One acrylic container was used for 100% and 70% cases individually. 16 testing points with various exposure times were made in a 4 by 4 array in an each container as shown in Fig. 18. The testing sequence started from left to right in the container, and then moved to the next row. Each point was 5 mm apart from

the other point. The complete samples are shown in Fig. 19. The pillar dimensions were measured at the end of the experiment using high-resolution images from top and side followed by measuring the pixel length.

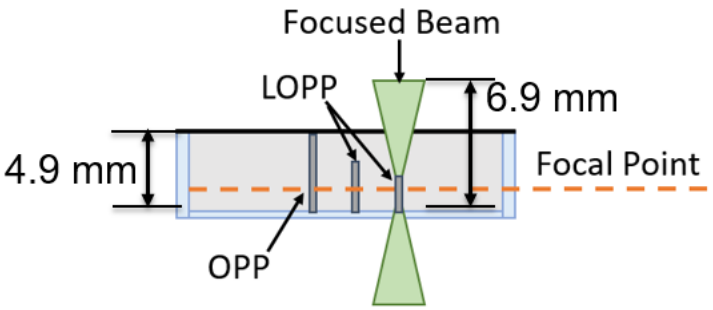

Figure 17. Schematic of OPP and LOPP effects on the structure growth.

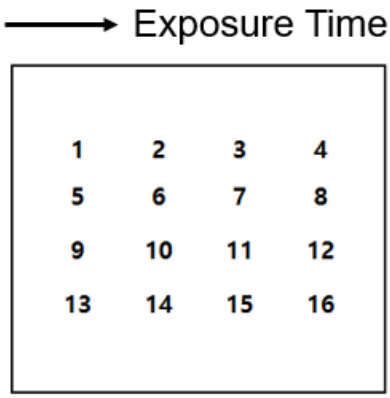

Figure 18. 4x4 matrix for the testing.

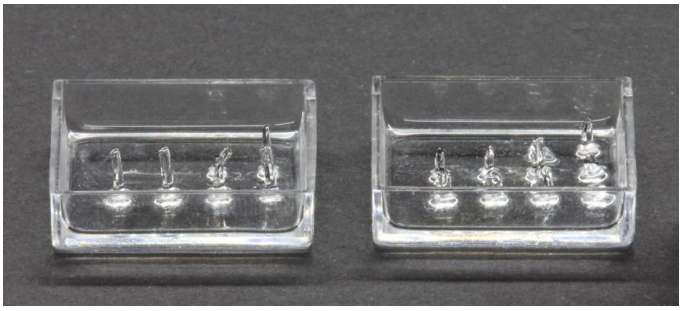

Figure 19. The cured pillars by 100% opening power (left) and 70% opening power (right).

3.2.2. Results

The results with 100% opening power are shown in Fig. 20 and 21. The exposure time was increased from 5 s to 80 s. There was no cured pillar until 50 s. At 55 s, the pillar was partially cured with a height of 2.2 mm near the focal point as shown in Fig. 20. It can be seen that the threshold for LOPP with 100% opening power has a narrow window between 50 s and 55 s. From the exposure time beyond 60 s, a full length pillar was observed through the resin depth, meaning an OPP effect. Except the exposure time of 55 s, the pillar height was around 4.5 and 4.7 mm. The 0.3 mm difference from the container depth could be due to the measurement error, the surface tension of the silicone resin, or slight buckling effect on the pillars without the hydrostatic force.

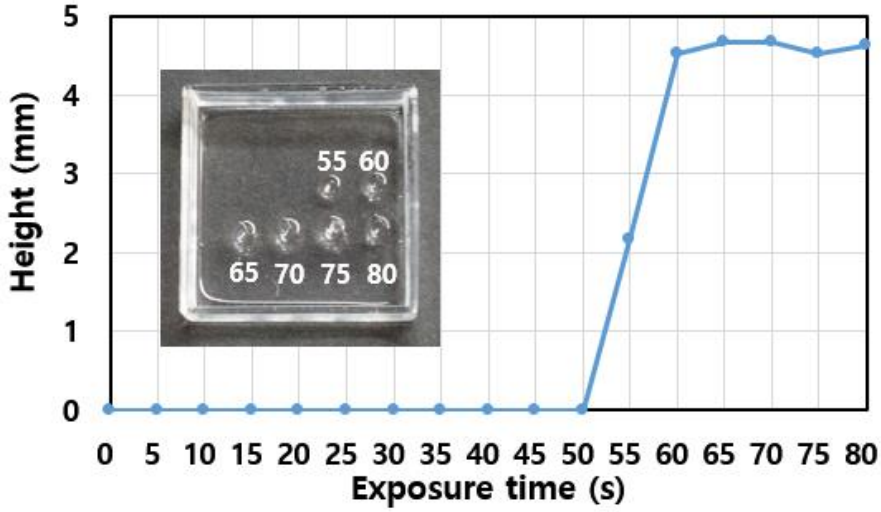

Figure 20. Results of 100% opening power: the pillar height vs. exposure time.

In addition to the pillar height, the diameter was also measured to observe the correlation with the exposure time. Note the pillar was not really in a perfect cylindrical shape, so the diameter was measured in an average sense. Fig. 21 shows a minimum

diameter of 0.5 mm at the exposure time 55 s, corresponding to the shorter pillar of 2.6 mm. From 60 s and onwards, the pillar diameter increased to about 1.2 mm; the maximum was 1.5 mm at the 80 s. It can be seen that once the pillar is formed, the dimensions do not change significantly with the exposure time.

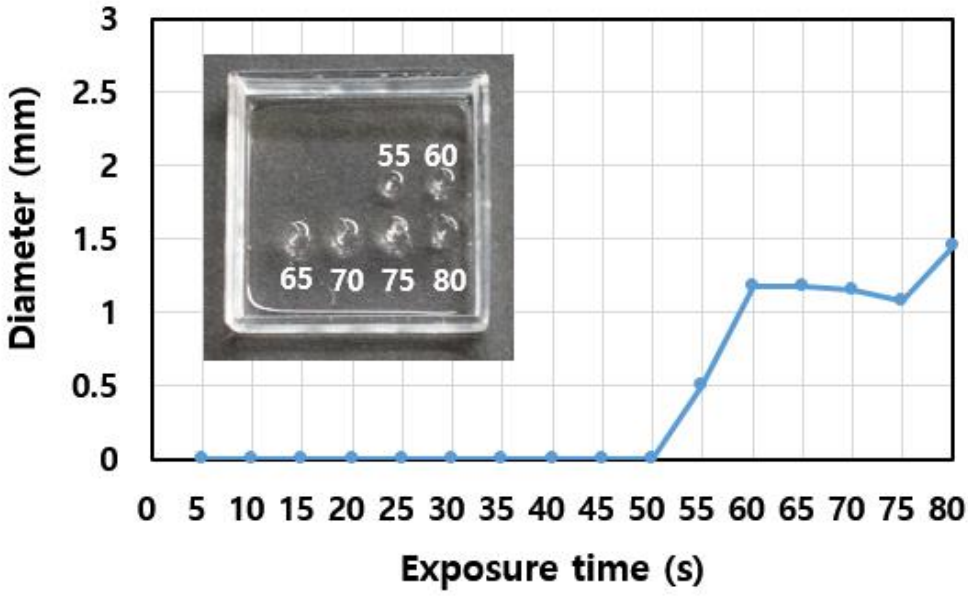

Figure 21. Results of 100% opening power: the pillar diameter vs. exposure time.

The results of 70% opening power are shown in Fig. 22 and 23. There were 5 s intervals for each point between 5 s to 50 s and 10 s intervals for each point between 50 s and 200 s. No pillar was cured between the exposure time 5 s and 100 s as shown in Fig. 22. The polymerization was observed at 110 s and beyond. The pillars at 110 s and 200 s collapsed prior to the measurements and thus marked as 0 mm in height. Compared to the 100% opening results, 70% shows more variations. The height varied from 1.3 mm (at 160 s) to 3.3 mm (at 150 s) though most of the pillars stayed around 2.6 mm level. Obviously, there existed a gap of 2.3 mm from the resin surface. This means an LOPP

effect that produces the pillars inside the silicone resin. Fig. 23 shows the measured diameter of the pillars. Unlike 100% case, there was an ascending trend with the increased exposure time. The minimum diameter was 1.3 mm at the exposure time of 120 s and the maximum was 2.4 mm at the 200 s.

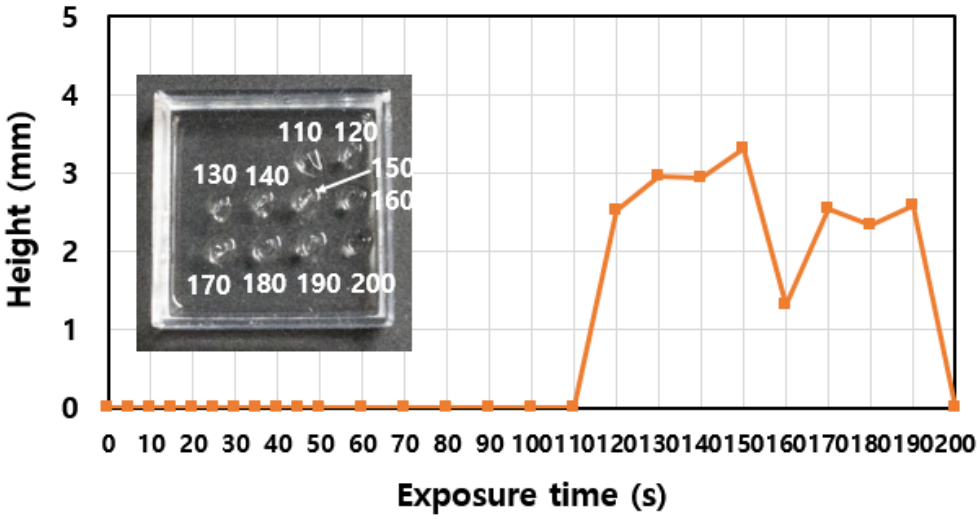

Figure 22. Results of 70% opening power: the pillar height vs. exposure time.

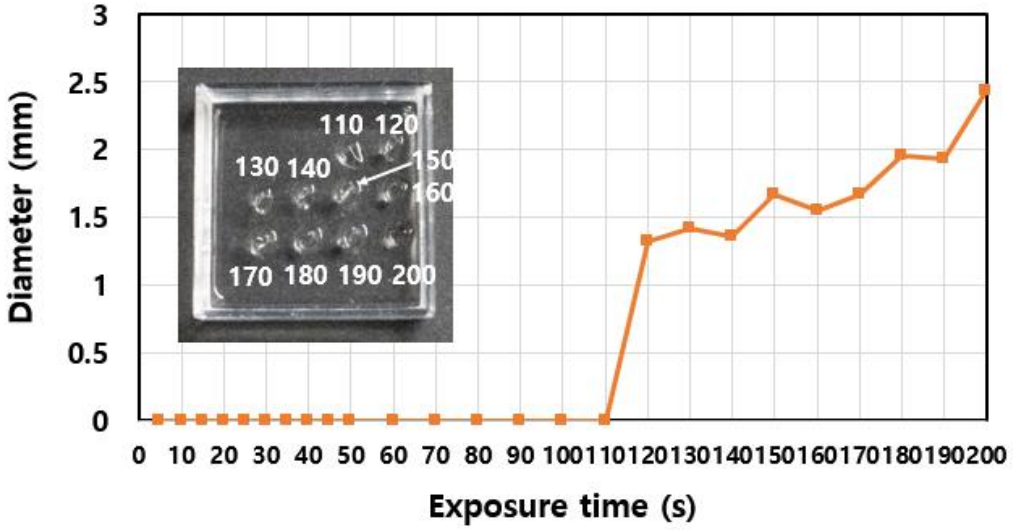

Figure 23. Results of 70% opening power: the pillar diameter vs. exposure time.

The average of the diameter was 1.7 mm, about 40% larger than those in the 100% opening power case. The low pillar height at 160 s could be due to an incomplete polymerization as a result of the unstable light source or locally lack of photo-initiators.

3.3. Discussion

LOPP can successfully cure the material in the middle of the silicone resin but the cured volume and shape are largely dependent on the UV light setup. Traditionally, the cured polymer volume is proportional to the total energy absorption (i.e., dose) under a uniform exposure. Following this hypothesis, Fig. 24 shows the calculation for the cured volume as a function of UV dose from the experimental results. The values of dose were calculated with actual irradiances measured by the radiometer and exposure times. The irradiance values were 381 mW/cm^2 for the 100% opening power and 272 mW/cm^2 for the 70% opening power. The cured volumes were estimated from the pillar height and diameter in the Results section. Interestingly, with 100% opening power, a lower dose is required to achieve the same cured volume as that needed for 70% opening power. This is because of a larger effective beam zone in 100% opening power than the 70% cases. This is also an evidence of the LOPP effect in the 70% opening power.

The cured geometries are quite different between two cases, in spite of a similar cured volume. The pillar is tall and thin in the case of 100 % opening power, and short and wide in the case of 70% opening power. This is a result of beam gradient that promotes polymerization in different directions.

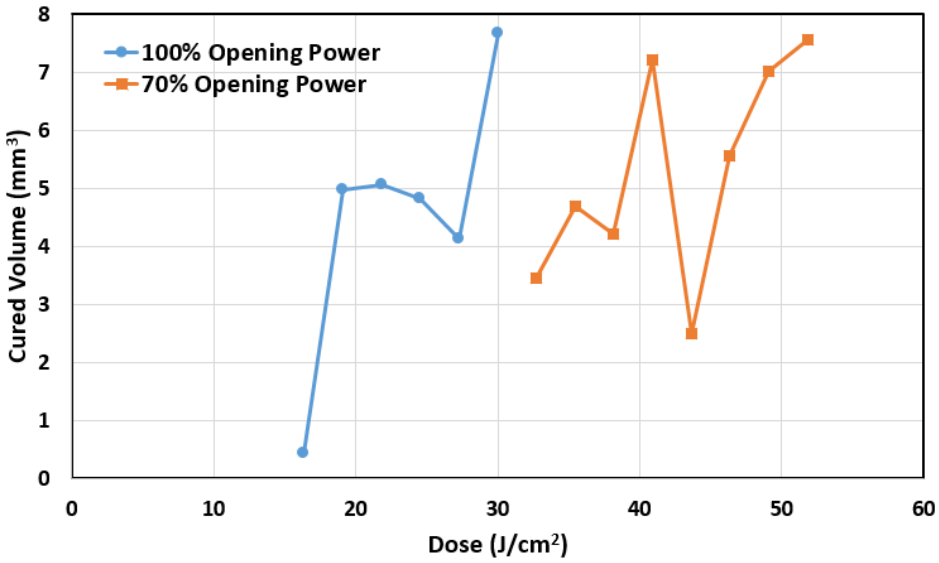

Figure 24. Dose vs Cured Volume for 100% and 70% opening power.

Figure 25 shows a schematic explanation for this phenomenon. An ideal graded light beam is in a shape of hourglass after passing the final lens of the optics setup. Around the focal point has the highest intensity where the polymerization can easily occur. This region is called effective beam zone. This zone is larger under 100% opening power due to a higher intensity as shown in Fig. 25 (a). As a result, the pillar tends to grow through the entire resin depth. In contrast, 70% opening power has a smaller (shorter) effective beam zone because of lower intensity, as shown in Fig. 25 (b). Thus, polymerization occurs only within a limited height.

As to the diameter difference, 70% opening power seems to cause more radial growth than that of the 100% opening power. This may be caused by material diffusions or beam transformation by cured parts. To understand the growth mechanism, more

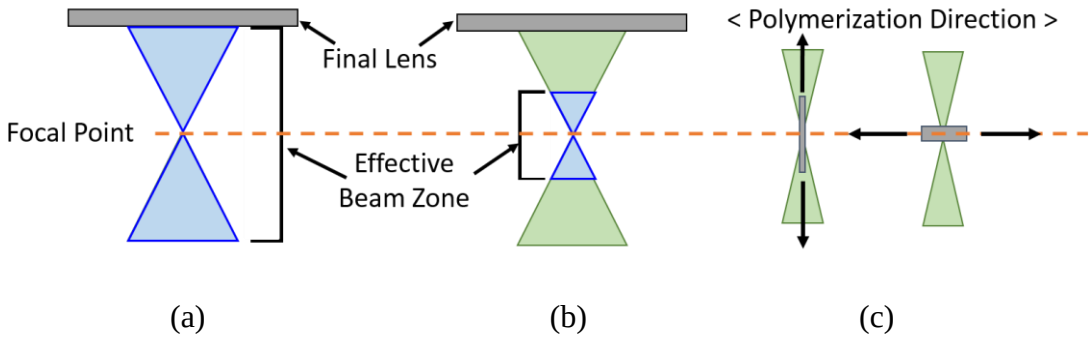

Figure 25. Schematics of effective beam zone depending on the opening powers (a) 100% opening power, (b) 70% opening power, (c) axial growth and radial growth

following studies are needed. Based on the observation in this study, the pillar of 70% opening power could be thin at the beginning and grow vertically. Because of the limited effective beam zone that inhibits the growth, a continuous UV exposure polymerizes the silicone resin around the cured volume, resulting in a wider pillar. The increasing trend of the diameter in Fig. 23 is an evidence of this phenomenon. Although the traverse growth is not observed in 100% power opening, it is believed that the pillar will eventually grow as the exposure time increases. The last measurement point at 80 s of Fig. 21 shows an increasing trend of the pillar diameter.

3.4. Conclusion

In this part, the qualitative observation and quantitative measurement were conducted to verify LOPP effect. The observation was based on trial-and-error for proof of LOPP concept. OPP and LOPP effects were observed depending on different intensities and exposure times. However, there was a vague boundary between LOPP and OPP effects due to the limitation of the optical setup. To distinguish LOPP and OPP

clearly, single-spot test was designed and conducted. The results from the test were quantitatively measured and analyzed. With 100% opening power, the threshold for LOPP has a narrow window. Beyond the threshold, the pillar grew up rapidly with full-height. With 70% opening power, LOPP effects were observed successfully. Due to relatively lower intensity than 100% opening power, LOPP was found with the entire exposure times. This means that controlling intensity with the specific wavelength is more practical to manage the exposure times to obtain more stable LOPP effect.

The maximum heights of pillars was 3.3 mm less than the depth of the container 4.9 mm. The shape of the pillars was different from the one of 100% opening power due to smaller effective beam zone that resulted in the limited heights.

Based on the qualitative observation and quantitative measurement, the printing with LOPP was designed and conducted. The details are presented in the next section.

4. FEASIBILITY STUDY OF PRINTING WITH LOPP

In this section, printing test with LOPP will be discussed. To verify the feasibility of the LOPP effect in printing process, the method and parameters were selected and conducted based on the results from the previous single-spot experiments. The printed samples were measured and analyzed by a surface profiler.

4.1. Parameter determination

A continuous printing was conducted to verify the LOPP effect in dynamic conditions. The process parameters for the printing were based on the results from the single-spot testing. However, the materials from the second batch were used in the continuous printing. Using the second batch could influence polymerization trends because they were non-commercial products. Therefore, the trends could be different from one of the previous experiment with the first material batch. To verify the trends of the second batch, the single-spot testing was carried out with the same method of the previous one.

In the single-spot testing, two levels of light intensity, 100% and 30% were used. The exposure time for 100% intensity was 30 to 180 s at 10 s increment and for 30% intensity was 90 to 127.5 s at 2.5 s increment. Each set of 16 testing points were made in a 4 by 4 array in an individual container as shown in Fig. 26. The testing sequence started from left to right in the container, and then moved to the next row. The pillars by LOPP were identified based on the height less than the resin depth, as same as the previous test.

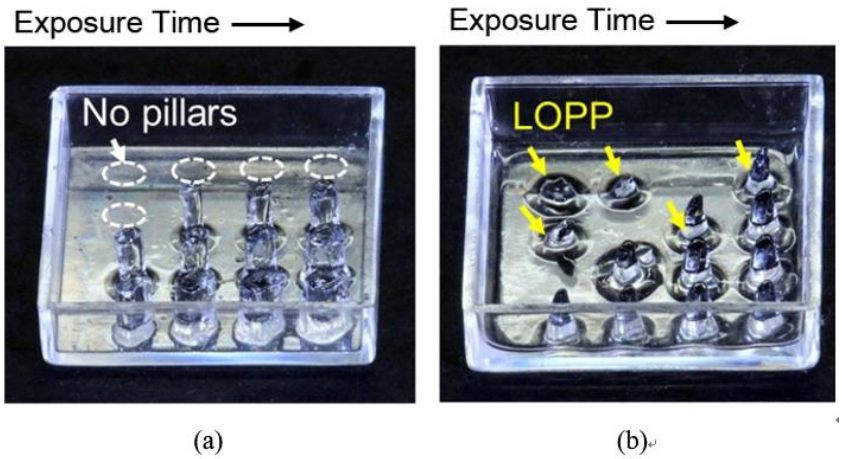

Figure 26. Results of the tests: (a) single-spot test at 100% intensity with only OPP pillars, (b) single-spot test at 30% intensity with both LOPP and OPP pillars.

The results with 100% opening power are shown in Fig. 26 (a). There was no cured pillar until the exposure time 50 s. From the exposure time beyond 60 s, full-length pillars were formed through the resin depth, meaning an OPP effect. LOPP effect was not found. As the exposure time increases, the diameter of pillars rapidly increases.

The results of 30% opening power are shown in Fig. 26 (b). 2.5 s were intervals for each point between 90 s to 127.5 s. From exposure time 90s, short pillars made by LOPP were observed. No pillar was formed at 95 s, 102.5 s and 110 s. The missing could be a lost during the drain due to weak adhesion to the bottom or no polymerization by unstable experimental conditions. The cone-shape pillars were observed for relatively taller pillars. It is significantly different from the cylindrical shape of the pillars made by OPP in 100% opening power. The optimal combination of the intensity and exposure time from the single-spot test was used for the continuous fabrication.

4.2. Printing test and result

In the continuous printing test, the parameters based on the stationary test were 30% light intensity and 125 s exposure time. Given the estimated focusing spot of 1 mm in diameter, the baseline feed rate was 0.5 mm/min. Three scaled feed rates were 0.667 (133%), 0.857 (171%), and 1.200 (240%) mm/min.

The focal point was set near the bottom for the adhesion to secure the parts. The beam was moved from left to right with displacement 15 mm and with each feed rate. Fig. 27 (a) and (b) show the volumetric lines produced by these feed rates and the surface topography measured by a surface profiler (Model G4, Alicona, Austria).

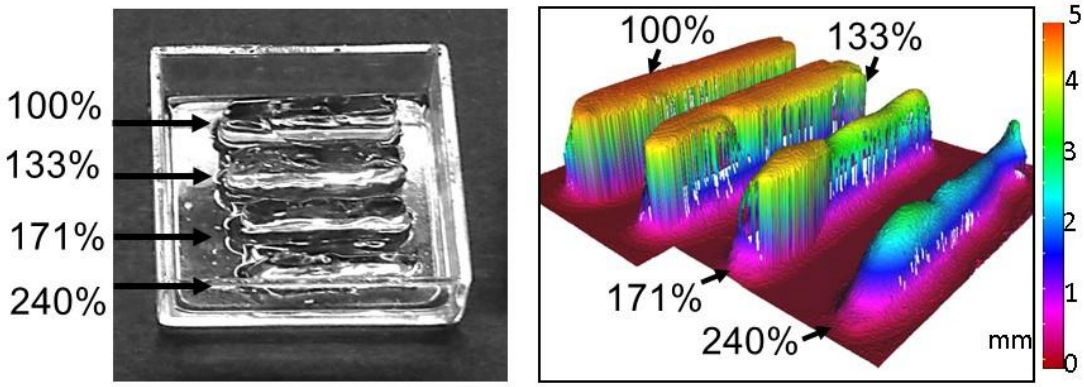

Figure 27. (a) Continuous printing test at 30% intensity and different feed rates (100% presents the baseline) and (b) measured profiles of (a).

Both the baseline feed rate and 133% speed created a full-height volumetric line, indicating an OPP effect. The 171% feed rate generated a nearly LOPP effect; 240% generated a complete LOPP structure. The height of the volumetric line was mostly less than 2.5 mm compared to the full-height of 4.8 mm. The 240% scale factor is equivalent to a 52 s exposure time, compared to the selected 125 s.

4.3. Discussion

The single-spot test with 30% opening power showed short pillars made by LOPP. Even for full-height pillars, the shape was conical, not cylindrical from OPP. This is because the great beam gradient created different energy distribution between 30% and 100% opening power. It means that 30% opening power in the 365 nm wavelength can initiate LOPP, OPP or both OPP and LOPP depending on the exposure time. Therefore, longer wavelengths than the 365 nm wavelength could achieve only LOPP less depending on the exposure time as shown in Fig. 28.

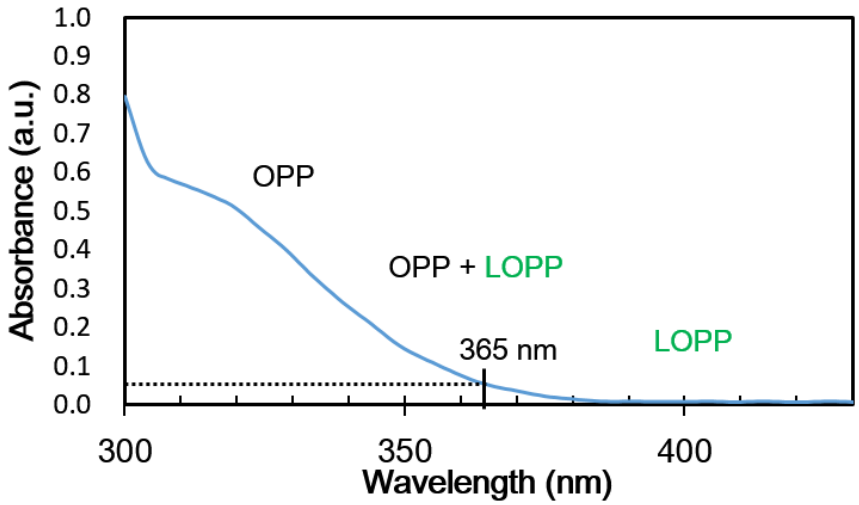

Figure 28. Three regions: OPP, OPP+LOPP and LOPP depending on wavelength in the absorbance spectrum.

In the printing test, the feed rate should be faster than the converted rate from the single-spot test. This is because the each beam exposure was overlapped in the printing motions as shown in Fig. 29 (a). With the increase by 71%, some partial areas of the volumetric line were made by LOPP effect. With the increase by 140%, the whole area were made by LOPP effect. This means that the increase by 71% is marginal for LOPP

effect. Therefore, further study between 71% and 140% or above could be conducted to understand the overlapped exposures. To estimate the overlapped exposure, the effective beam zone at the focal point, so called voxel, should be studied as shown in Fig. 29 (b). The voxel has a non-uniform distribution depending on wavelength, intensity, exposure time and optical setup. The voxel size can influence on process resolution. In addition, the voxel shape can impact on part integrity deteriorated by structural defects such as voids and overcuring as shown in Fig. 29 (a).

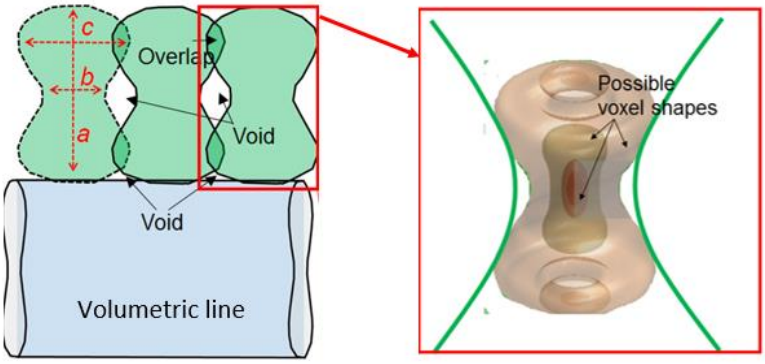

Figure 29. (a) Overlaps of the voxel, (b) numerically estimated voxel shape [20].

4.4. Conclusion

The printing test was conducted and analyzed to prove the feasibility of the LOPP in the process. Single-spot test was repeated to confirm the polymerization trend because the materials were used from the different batch. In the test, 30% opening power in the 365 nm wavelength could initiate LOPP, OPP or both OPP and LOPP depending on the exposure time. It indicates longer wavelengths than the 365 nm wavelength could achieve only LOPP less depending on the exposure time.

For the printing test, the proper exposure time from the single-spot test was chosen and converted to feed rate. From the experimental results, the equivalent factor between the single-spot test and the printing test was 240% scale factor due to overlapped beam exposure in the printing. To understand the beam exposure, voxel formation should be studied because the size and the shape of the voxel plays key roles in process resolution and part integrity.

5. CONCLUSIONS AND FUTURE WORKS

In this section, major conclusions will be presented and future works will be discussed based on the conclusions.

5.1. Conclusions

In this paper, hydrostatic 3D-Printing (H3P) was proposed and demonstrated to overcome the low shape stability issue of soft materials in additive manufacturing. The key of the concept is in-liquid polymerization to secure the hydrostatic condition during the fabrication process. Low one-photon polymerization (LOPP) was utilized for in-liquid polymerization. There are two requirements to achieve LOPP. The first one is to use the wavelength with a low absorbance rate by the materials. 365 nm wavelength was used with 0.051 absorbance rate by the material in the study. The second one is to create a great beam gradient for maximizing the low absorbance rate. It can be realized by a lens with a high numerical aperture (N.A.). However, a high N.A. results in a short focal length of the lens as a trade-off. The final lens with N.A. = 1 and focal length 6.9 mm was used in the study.

With the test bed, the feasibility studies for LOPP in H3P were conducted with the qualitative observation and quantitative experiments. OPP and LOPP effects were successfully observed depending on different intensities and exposure times. The intensity must be low enough to produce LOPP structures inside of the resin regardless the exposure time. This means that controlling intensity with the specific wavelength is more practical to manage the exposure times to obtain more stable LOPP effect.

Therefore, the parameter selection should follow the priorities of wavelength, light intensity, and then exposure time.

In printing test, the feed rate based on the stationary test should be scaled up to create the structures by LOPP effect. Because the non-uniform beam distribution causes the overlapped beam exposure. To predict the beam exposure, voxel formation should be studied. The size and the shape of the voxel plays key roles in process resolution and part integrity. The current resolution is about 2 mm. A better resolution might be achieved with longer wavelengths and more precise optics. The details will be discussed in the future works.

5.2. Future works

Low one-photon polymerization can successfully achieve in-liquid polymerization for hydrostatic 3-D printing. However, furthermore studies should be conducted to complete the precise and stable 3D printing process. First of all, a longer wavelength than 365 nm with a lower absorbance rate could be tested to improve the LOPP effect. Depending on the absorbance rate, the process stability and resolution could be enhanced. In addition, voxel formation should be studied to understand the non-linear beam distribution. The size and the shape of the voxel plays key roles in process resolution and part integrity. An experiment and a simulation for the voxel formation will be conducted as one of the future works. To be specific, to simulate the voxel formation, the effective light intensity distribution and the curing threshold must be studied. The intensity distribution describes where the polymerization takes place at what rate; the curing

threshold defines the time to fully cure a unit volume. Therefore the voxel formation can be modeled with two information.

The effective light intensity distribution should consist of two models. The first model is called exposure model and the second one is absorption model. As shown in Fig. 30(a), the exposure model determines the effective exposure along the beam path.

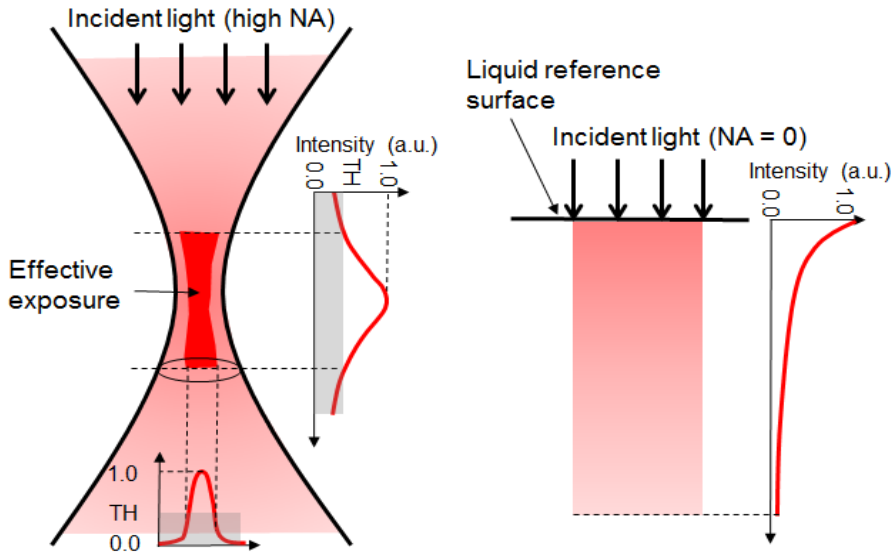

(a) (b)

Figure 30. (a) Exposure model and (b) absorption model.

Assuming a graded beam with high NA after the objective lens, the intensity should reach the maximum at the focal point along the axial direction and then decades. In the radial direction at any cross-section, the light should follow a Gaussian distribution. This phenomenon is called Airy disk [21]. Since the light intensity distribution is non-uniform within the light beam, it is typically described by the 3D point spread function *PSF*(*x*, *y*, *z*), where *x*, *y*, and *z* identify a given point inside the light beam [22]. Polymerization requires to break the bond of photo initiators, and thus it needs certain intensity at a

given wavelength. By knowing the intensity threshold (*TH*), the effective exposure region can be mapped as $E(x, y, z)$. Then, the effective light intensity distribution can be calculated by the convolution between *PSF* and *E*, denoted by $I(x, y, z)$. Only the non-zero point can initiate the polymerization. However, in reality, the light intensity distribution is not symmetric in the axial direction because part of the incident light is absorbed by the photo initiators. Therefore, an absorption model will be added. The Beer-Lambert law is adopted for the absorption model which describes the attenuation of light as it propagates through the material [23]. Light transmitted through a layer of material with thickness z has an intensity of $J(z) = J_0 \cdot e^{-\alpha z}$, where J_0 is the intensity of incident light and α is the attenuation (or absorption) coefficient of a polymer under certain wavelength. Therefore, to accurately model the effective light intensity, it needs to be modified by multiplying e^{-az}.

The entire light beam can be meshed with identical small cubes of volume *V*, as shown in Fig. 31. The time to cure the entire area can be described with the dosage to fully cure this volume under a given wavelength. Then voxel formation, including nucleation and growth can be simulated.

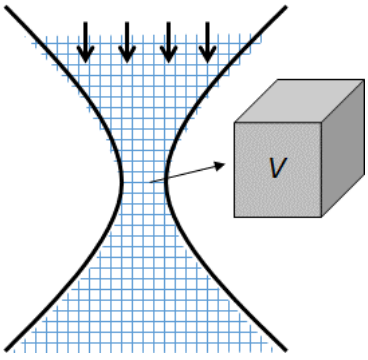

Figure 31. Mesh of the light beam.

Lastly, the hydrostatic condition was not thoroughly discussed in this study due to the difficulty observing the transparent structure inside the liquid. In general, the ideal polymer for hydrostatic printing should have a nearly identical density before and after curing to achieve zero gravity environment, and a high viscosity to minimize the motion as a result of density change.

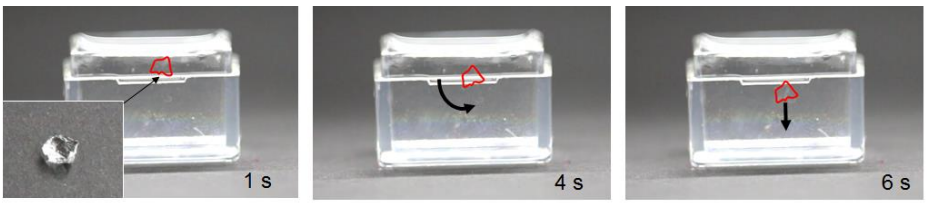

Figure. 32 An example of motions by density difference inside the liquid over time

If the concept of H3P is successful, the soft material fabrication could be realized without physical support structures or less. However, if there is a density difference before and after curing, the cured part could move both rationally and translationally during the process as shown in Fig. 32. Therefore, the parameters for hydrostatic condition should be investigated. Experimental and numerical methods will be conducted. Firstly, the model with smoothed-particle hydrodynamic (SPH) and finite element method (FEM) will be used as shown in Fig. 33.

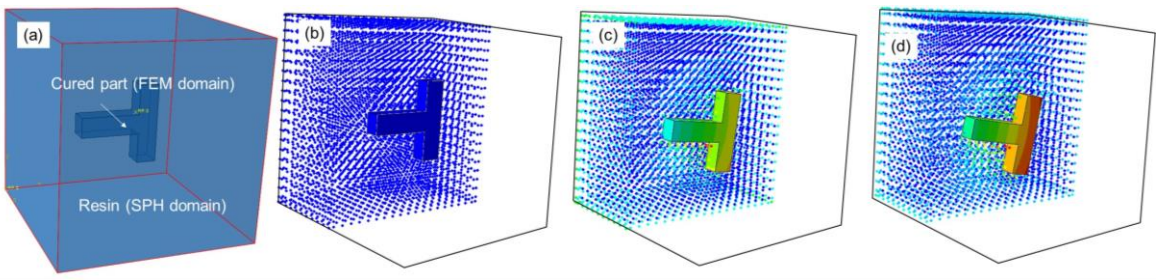

Figure. 33 Preliminary study of SPH-FEM simulation of the part motion in a hydrostatic condition: (a) model setup, (b) initial status at 0 s, and motion at (c) 1 s and (d) 2 s from the cross-section view of the model. Color contour shows the level of displacement magnitude.

The results from the simulation will be compared with the ones from the experiments. In addition, the part motion and the associated dimensional errors in the final part will be studied.

In conclusion, with the future works, hydrostatic 3-D printing process will be thoroughly understood and precisely estimated to achieve stable printing quality and high resolution.

REFERENCES

1. Muroi, H., et al., *Development of Optical 3D Gel Printer for Fabricating Free-Form Soft & Wet Industrial Materials and Evaluation of Printed Double-Network Gels.* Journal of Solid Mechanics and Materials Engineering, 2013. **7**(2): p. 163-168.

2. O'Brien, F.J., *Biomaterials & scaffolds for tissue engineering.* Materials Today, 2011. **14**(3): p. 88-95.

3. Kohane, D.S. and R. Langer, *Polymeric Biomaterials in Tissue Engineering.* Pediatr Res, 2008. **63**(5): p. 487-491.

4. Place, E.S., et al., *Synthetic polymer scaffolds for tissue engineering.* Chemical Society Reviews, 2009. **38**(4): p. 1139-1151.

5. Wood, R. and C. Walsh, *Smaller, Softer, Safer, Smarter Robots.* Science Translational Medicine, 2013. **5**(210): p. 210ed19.

6. Laurent, M., et al., *Clinical evaluation of the marginal fit of cast crowns – validation of the silicone replica method.* Journal of Oral Rehabilitation, 2008. **35**(2): p. 116-122.

7. FrippDesign, *The Future of Prosthetics: 3D printed nose, ear and eye*. 2013, www.3ders.org.

8. Hicks, J., *Get Ready to Doodle With The First 3D Drawing Pen*, in *Forbes*. 2013.

9. Chen, C. and M. Wettergreen, *Diagram of Selective Laser Sintering*. 3D Systems, Inc.

10. Klimas, L., *The 3D Printing Pen That Draws in the Air Might Be Your Childhood Dream Come True*. 2013, The Blaze.

11. Jacobs, P.F. *Fundamentals of stereolithography*. in *Proceedings of the Solid Freeform Fabrication Symposium*. 1992.

12. Zhang, A.P., et al., *Rapid fabrication of complex 3D extracellular microenvironments by dynamic optical projection stereolithography.* Advanced materials, 2012. **24**(31): p. 4266-4270.

13. Chen, C. and M. Wettergreen, *Diagram of Sterolithography*. 3D Systems, Inc.

14. Pan, Y., C. Zhou, and Y. Chen, *A Fast Mask Projection Stereolithography Process for Fabricating Digital Models in Minutes.* Journal of Manufacturing Science and Engineering, 2012. **134**(5): p. 051011-051011.

15. Dorkenoo, K.D.H., et al., *Monitoring the Contractile Properties of Optically Patterned Liquid Crystal Based Elastomers.* 2012.

16. Denk, W., J.H. Strickler, and W.W. Webb, *Two-photon laser scanning fluorescence microscopy.* Science, 1990. **248**(4951): p. 73-76.

17. Kawata, S., et al., *Finer features for functional microdevices.* Nature, 2001. **412**(6848): p. 697-698.

18. Li, Q., et al., *Concept for three-dimensional optical addressing by ultralow one-photon absorption method.* Optics Letters, 2013. **38**(22): p. 4640-4643.

19. Do, M.T., et al., *Submicrometer 3D structures fabrication enabled by one-photon absorption direct laser writing.* Optics Express, 2013. **21**(18): p. 20964-20973.

20. Lai, N.D., *One-photon absorption excitation for high-resolution nanoscopy.* SPIE Newsroom, 2014.

21. Airy, G.B., *On the Diffraction of an Object-glass with Circular Aperture.* Transactions of the Cambridge Philosophical Society, 1835. **5**: p. 283-291.

22. Wan, X. and R. Menon, *Proximity-effect correction for 3D single-photon optical lithography.* Applied Optics, 2016. **55**(3): p. A1-A7.

23. Beer, *Determination of the absorption of red light in colored liquids.* Annalen der Physik und Chemie, 1852. **86**: p. 78–88.